

**NATIONAL RADIO ASTRONOMY OBSERVATORY**  
**Charlottesville, Virginia**

**ELECTRONICS DIVISION INTERNAL REPORT NO. 326**

**Summary of January 2015 PAF observations with the  
GBT, Results and Comparison with PAF model**

D. Anish Roshi<sup>1</sup>, William Shillue<sup>1</sup>, J. Richard Fisher<sup>1</sup>, Steve White<sup>2</sup>,  
Robert Simon<sup>2</sup>, Karl F. Warnick<sup>3</sup>, Brian Jeffs<sup>3</sup>

<sup>1</sup> National Radio Astronomy Observatory, Charlottesville,

<sup>2</sup> National Radio Astronomy Observatory, Green Bank,

<sup>3</sup> ECE Dept., Brigham Young University, Provo, UT, USA

March 16, 2015

# Summary of January 2015 PAF observations with the GBT, Results and Comparison with PAF model

D. Anish Roshi<sup>1</sup>, William Shillue<sup>1</sup>, J. Richard Fisher<sup>1</sup>, Steve White<sup>2</sup>,  
Robert Simon<sup>2</sup>, Karl F. Warnick<sup>3</sup>, Brian Jeffs<sup>3</sup>

<sup>1</sup> National Radio Astronomy Observatory, Charlottesville,

<sup>2</sup> National Radio Astronomy Observatory, Green Bank,

<sup>3</sup> ECE Dept., Brigham Young University, Provo, UT, USA

March 16, 2015

Version 2.0

## Revision History

Version 1.0: February 20, 2015. with results mostly from Virgo A data set; PAF model  $\frac{T_{sys}}{\eta}$  vs frequency results presented.

Version 2.0: March 11, 2015. Results from data set obtained toward calibrators 3C286, 3C484, 3C353 included. PAF model  $\frac{T_{sys}}{\eta}$  vs offset from boresight result included.

## Abstract

This document summarizes the measurements of the L-Band Cryogenic Phased Array Feed (PAF) Receiver made in January 2015 at the Green Bank Outdoor Test Facility (OTF) and on the Green Bank Telescope (GBT). The report includes details about the receiver and system configuration, engineering and science tests performed, performance of the receiver individual channels and the beamformed results, performance versus frequency, quality of the off-axis beams, and comparisons with the PAF electromagnetic model. Some of the results to note are:

- The median  $\frac{T_{sys}}{\eta}$  measured on the GBT is 45.5 K near 1550 MHz.
- The  $\frac{T_{sys}}{\eta}$  increase for off-axis beams spaced at 1 full-width half-maximum (FWHM) spacing was 13K, increasing from 50K to 63K at 1 FWHM beamwidth (7'.2) offset from boresight at 1700 MHz.
- The modeled results predict well the measured  $\frac{T_{sys}}{\eta}$  vs offset from boresight direction but needs an increase in receiver temperature of about 8K to match the measured results. Additionally, there is an increase of about 5K in receiver temperature that came from the use of replacement transistors in the low-noise amplifiers. The model also predicts the measured  $\frac{T_{sys}}{\eta}$  vs frequency with the additional increase in receiver temperature mentioned above.
- Future work will include test and analysis to understand the remaining mismatch between the model and the results, and the use of improved cryogenic LNAs.

# 1 Experimental setup, Observation and Data analysis

A 19-element dual-polarized array with "Kite" dipoles was used for the observations. The array was located at the prime focus of the GBT during observations. Images of the "Kite" dipole and the array are shown in Fig. 1. The array elements were designed using an optimization process. The design began by identifying a suitable isolated dual-pol crossed dipole of input impedance of  $50 \Omega$  using a full-wave EM model. A "kite" design was selected as the best combination of manufacturability and adjustable degrees of freedom for tuning. An infinite array model was then used to estimate the embedded array element active impedance, which accounts for array mutual coupling effects. A genetic algorithm was used to tune the design to achieve active impedance matched to the cryogenic LNA noise parameters. An initial hexagonal seven element array is then obtained from the infinite array model. The seven element array was further optimized to re-tune the active impedance to the LNA noise parameters. Finally, the element design was embedded in a nineteen element array and optimized to achieve an active impedance match and maximum sensitivity over the PAF field of view. Throughout the optimization process, seven geometrical parameters of the element were allowed to vary: the length of the kite arm from feed to center tip, the length of the kite arm from feed to outside tips, the thickness of the arms, the separation of the feed point and ground plane, the radius of the conductor feeding the coax line, the angle of kite sweep, and the angle of the kite from horizontal (the angle between the arms and support posts). For further details, see Warnick et al. (2011).

A block diagram of the PAF receiver system and backend used for observations is shown in Fig. 2. The first stage cryogenic temperature is maintained at 15 K, which is the physical temperature of the LNAs. The signals are amplified and transmitted through a fiber optic system using analog modulation. A built in provision to inject an external signal to all the 38 analog channels is present in the receiver system. During observations, the signal from GBT's frequency synthesizer in the focal cabin was connected as the external calibration signal injected after the LNA's, and the frequency of this signal was tuned to the center of the observing band. This calibration signal was normally off during the GBT measurements. An analog link consisting of a fiber optic transmitter and receiver pair is used to transfer the RF signals from the GBT to the GBT control room, where a two-stage down-converter follows the analog fiber receiver system. The local oscillator (LO1) of the first stage down-converter is tunable. The LO for the second stage down-converter (LO2) is fixed at 393.0 MHz during the observations.

The Data Acquisition System (DAQ) consists of 10 computers (referred to as paf1 through paf10) each having a card with 4 ADCs. Thus, signals can be digitized from a total of 40 channels, out of which 38 channels are used by the 19-element dual-polarized PAF. The DAQ records 8 bit quantized voltages, sampled at 1.25 Msps, from all of the 40 signal paths. The desired RF frequency is tuned to the center of the digitized band using LO1. A tone burst is injected at the beginning of the data acquisition to calibrate the relative phase between ADC sampling clocks in different computers. For the calculation of the correlation products, we developed Python and C++ code in-house. Programs in this package first transfer the data from paf1 through paf10 to the data processing computer paf0. Each set of 10 data files from paf1 through paf10 is then collated in a single file. Because the sample clock in each ADC card uses a divide-by-two frequency divider, there is a half-clock-cycle ambiguity in the relative clock phases of the ten ADC cards. This ambiguity is different from one scan to the next. The correlator program in the package uses the tone burst to estimate the relative phase offsets between ADC clocks and put these offset values in the header of the final correlation product FITS file. The correlator program then skips the tone burst part of the sampled data and then computes and averages a series of 256 point FFTs of the time series. The spectral resolution of the voltage spectra is 4.9 KHz. The time average of self-

and cross-products of these voltage spectra provide the correlation products, which are written to a FITS file. A maximum signal-to-noise ratio beamformer algorithm is implemented in Python and Matlab, which is then used to get the beamformed data products.

Initial receiver and system tests were done using the Green Bank Outdoor Test Facility (OTF) on 14th January 2015. Green Bank Telescope observations with PAF were done during 25 and 26 January 2015 (UT dates). The PAF cryostat failed for the 26 January observations resulting in elevated receiver temperature. We later verified that the observations on 25 January were not affected by cryostat failure by taking a short data set on 30 January 2015, after the receiver was re-pumped and cooled to 15K. The 30 January data and 25 January data matched well. During the observing period, calibrator sources Virgo A, 3C286, 3C348 and 3C353 were observed. Table 1 gives a summary of system configuration and data analysis software used during January 2015 PAF test. For comparison, we have included the details of g efficiency in December 2013 PAF test configuration in Table 1. Note that the December 2013 tests were compromised by excess unwanted sideband leakage in the second mixer stage which was fixed by retuning the second LO in the 2015 measurements. Table 2 is a summary of the log of January 2015 measurements and Table 3 gives the observed positions of sources and off-source regions.

## 2 Receiver Temperature

The data taken on 14 January 2015 (see Table 2) were used to estimate the receiver temperature of the PAF. The receiver temperature can be written in terms of the Y factor as

$$T_{rec} = \frac{T_{hot} - YT_{sky}}{Y - 1} \quad (1)$$

where

$$Y = \frac{\mathbf{w}^H \mathbf{C}_{hot} \mathbf{w}}{\mathbf{w}^H \mathbf{C}_{cold} \mathbf{w}}. \quad (2)$$

$\mathbf{C}_{hot}$  and  $\mathbf{C}_{cold}$  are the correlation matrices obtained on ‘hot’ load and ‘cold’ sky respectively.  $T_{hot}$  (= 300 K) and  $T_{sky}$  (= 8 K) are the ‘hot’ load and ‘cold’ sky temperatures respectively and  $\mathbf{w}$  is the weight vector. The ‘hot’ load was an absorber pad that covered the array and a metal cone that blocked leakage around the edge of the absorber. This equation can be used to determine the beamformed receiver temperature, but here we use it to determine the individual dipole-channel receiver temperatures by setting the weight corresponding to that dipole to 1 and all other dipoles 0. Plots of the receiver temperature of the 19 “X” and 19 “Y” polarization dipoles and the median temperature of all the 38 dipoles are shown in Fig. 3. The median receiver temperature is about 25 K at 1.7 GHz.

## 3 GBT observations: data quality check

We use the ‘grid observation’ made toward Virgo A to assess the quality of the data obtained during January 2015 observations. For ‘grid observations’ the telescope pointing were shifted in elevation and cross-elevation by 2’ on a tangent plane centered on Virgo A (see Fig. 4). Due to overhead in data acquisition and antenna motion, the total time taken to complete these observation is about 2.5 hrs. The observations were made at 1.7 GHz. We obtain the beam pattern corresponding to the signals from each dipole (ie by setting the weight of a dipole to 1 and all other dipoles to 0) from this data set (see Fig. 5). Since the grid center need not be at the peak of this beam pattern, the peak value is not sampled in all cases. A plot of the maximum ratio of the dipole antenna temperature

Table 1: System configuration/analysis software for Dec 2013 and January 2015 PAF test

	Dec 2013 Test	Jan 2015 Test	Reference
FLAG Receiver	19x2 element FLAG PAF receiver. LNAs with replacement transistors. Kite dipoles	19x2 element FLAG PAF receiver. LNAs with replacement transistors. Kite dipoles	Note [1]
Analog Fiber Optic Transmitters	Transmitter LRT-L1-6M-03-S1550L Receiver LRR-L1-6M-04L	Transmitter LRT-L1-6M-03-S1550L Receiver LRR-L1-6M-04L	Note [2]
Calibration Tone Input	No input connected	Tone input connected	Note [1]
GBT Fiber Optics	Possible issues with excess fiber loss during test	No fiber issues during test	Note [3]
Dipole Type, Orientation/Polarization	Kite dipole, dipoles oriented 45-deg with respect to elevation axis	Kite dipole, dipoles oriented 45-deg with respect to elevation axis	Note [4]
System and Electronics	Analog Fiber Link, analog downconverters, 0.42 MHz IF bandwidth	Analog Fiber Link, analog downconverters, 0.42 MHz IF bandwidth	Note [5]
Data Acquisition	ADLink Data Acquisition System	ADLink Data Acquisition System	Note [6]
Acquisition Software	Acq.py (acquire data) Paf_check.py (check data)	Acq.py (acquire data) Paf_check.py (check data)	Note [7]
Telescope Control software	GBT M&C system	GBT M&C system	Note [8]
Correlator Software	Various python programs for collating and processing data	Various python programs for collating and processing data	Note [9]
Beamforming and Analysis Software	Fullpolbeamformer.py	Fullpolbeamformer.py rayleighbf.py	

Note 1 - Preliminary Report on Dec 2013 GBT Test at PAF Wiki: <https://safe.nrao.edu/wiki/bin/view/Main/PafDevelop>

Note 2 - Vialite Fiber Link manual : <https://safe.nrao.edu/wiki/pub/Main/PafDevelop/VIALITE.pdf>

Note 3 - The Dec 2013 had suspect channels due to fiber issues. The 2015 test did not. See [https://safe.nrao.edu/wiki/pub/Main/PafDevelop/Record\\_of\\_Fiber\\_Issues\\_for\\_GBT\\_Testing\\_of\\_Dec\\_2013\\_and\\_Jan\\_2015.pdf](https://safe.nrao.edu/wiki/pub/Main/PafDevelop/Record_of_Fiber_Issues_for_GBT_Testing_of_Dec_2013_and_Jan_2015.pdf)

Note 4 - PAF 1300-1800 MHz Receiver element Mapping, 9/5/13, B. Simon, <https://safe.nrao.edu/wiki/pub/Main/PafDevelop/PAFmapping2.pdf>

Note 5 - [https://safe.nrao.edu/wiki/pub/Main/PafDevelop/Block\\_diagram.pdf](https://safe.nrao.edu/wiki/pub/Main/PafDevelop/Block_diagram.pdf), [https://safe.nrao.edu/wiki/pub/Main/PafDevelop/PAF\\_block\\_diagram\\_02.pdf](https://safe.nrao.edu/wiki/pub/Main/PafDevelop/PAF_block_diagram_02.pdf)

Note 6 - <https://safe.nrao.edu/wiki/pub/Main/PafDevelop/ProcessingADLinkData.pdf>

Note 7 - [http://www.cv.nrao.edu/~rfisher/ArrayFeed/paf\\_adlink\\_stand\\_alone.html](http://www.cv.nrao.edu/~rfisher/ArrayFeed/paf_adlink_stand_alone.html)

Note 8 - <http://www.gb.nrao.edu/GBT/MC/doc/designReview/designReview.html>

Note 9 - [http://www.cv.nrao.edu/~rfisher/ArrayFeed/software\\_correlator.html](http://www.cv.nrao.edu/~rfisher/ArrayFeed/software_correlator.html)

Table 2: Observation log

Project	UT Date of Obs	Description
TGBT15A_000_06	14 Jan 2015	Scans 1 to 61 Hot load data for freq 1250 to 1850 MHz in increments of 10 MHz. Scans 62 to 122 Cold Sky data for freq 1250 to 1850 MHz in increments of 10 MHz.
TGBT14B_913_02	25 Jan 2015	Scans 25 to 48 On/Off on Virgo A; freq 1250 to 1800 MHz in steps of 50 MHz Scans 49 to 489 grid obs; source Virgo A; freq 1700 MHz Scans 574 to 597 On/Off on Virgo A; freq 1250 to 1800 MHz Scans 598 to 621 On/Off on 3C286; freq 1250 to 1800 MHz Scans 622 to 645 On/Off on 3C348; freq 1250 to 1800 MHz Scans 646 to 669 On/Off on 3C353; freq 1250 to 1800 MHz Scans 670 to 741 On/Off at 6 offset (4' offset) positions centered on Virgo A; freq 1250 to 1800 MHz
TGBT14B_913_05	30 Jan 2015	Scans 9 to 81 On/Off at 6 offset (4' offset) positions centered on Virgo A; freq 1250 to 1800 MHz

Table 3: Observed sources and off-source positions

Source	J2000 coordinates		Off-source position	
	RA(2000)	DEC(2000)	RA(2000)	DEC(2000)
VirgoA	12:30:49.6	+12:23:21.0	12:30:49.6	+13:23:21.0
3C286	13:31:08.3	+30:30:33.0	13:33:08.3	+30:30:33.0
3C348	16:51:08.3	+04:59:26.0	16:55:08.3	+04:59:26.0
3C353	17:20:29.5	-00:58:52.0	17:24:29.5	-00:58:52.0

to system temperature in the data set is shown in Fig. 4. A major cause of the variation of this ratio is that the peak response is not sampled in the ‘grid observation’. The dipole power relative to a reference grid position in dB is shown in the rightmost plot in Fig. 4. The variation of power measured on cold sky is less than 0.5 dB over 2.5 hrs.

## 4 $\frac{T_{sys}}{\eta}$ and $T_{rec}$ vs frequency

Observations made toward Virgo A, 3C286, 3C348 and 3C353 were used to estimate the performance of the PAF. The performance is expressed as the ratio  $\frac{T_{sys}}{\eta}$ , where  $T_{sys}$  is the system temperature and  $\eta$  is the aperture efficiency. This ratio is obtained after forming beams as follows. The observation toward a source provides an on-source power, which is given by  $\mathbf{w}^H \mathbf{C}_{on} \mathbf{w}$ . Here  $\mathbf{C}_{on}$  is the correlation matrix obtained from signals from PAF output and  $\mathbf{w}$  is the weight vector. An off-source power,  $\mathbf{w}^H \mathbf{C}_{off} \mathbf{w}$ , is measured by moving the telescope away from the source. Here  $\mathbf{C}_{off}$  is the correlation matrix measured at the off-source position. The signal-to-noise ratio (SNR) is then

$$\text{SNR} = \frac{\mathbf{w}^H \mathbf{C}_{on} \mathbf{w}}{\mathbf{w}^H \mathbf{C}_{off} \mathbf{w}} - 1. \quad (3)$$

For beamforming, a solution to the weight vectors in Eq. 3 is obtained by maximizing the SNR. This method of forming beams is referred to as maximum SNR beamforming. The solution for the weight vectors is obtained from the eigenvector corresponding to the maximum Rayleigh quotient and the maximum Rayleigh quotient gives the maximum SNR.

The maximum SNR in Eq. 3 gives maximum  $\frac{T_a}{T_{sys}}$ , where  $T_a$  is the excess antenna temperature due to the source and  $T_{sys}$  is the cold sky system temperature, and both are values obtained after forming the beam. The antenna temperature is related to the aperture efficiency through the equation

$$\frac{1}{2} SA \eta = k T_a, \quad (4)$$

where  $S$  is the flux density of the source,  $A$  is physical area of the GBT and  $k$  is the Boltzmann constant. Combining Eq. 3 and Eq. 4 we get

$$\frac{T_{sys}}{\eta} = \frac{\frac{1}{2} SA}{k \text{SNR}_{max}} \quad (5)$$

where  $\text{SNR}_{max}$  is the maximum SNR. As seen from Eq. 5 the measured  $\frac{T_{sys}}{\eta}$  depends on the flux density of the source. Flux density models for Virgo A and 3C286 are shown in Fig. 6. The model for Virgo A is taken from Baars et al. (1977). For 3C286, we used the latest model given by and Perley & Butler (2013). These flux density values are accurate to better than 5%. The difference in flux densities between Baars et al. (1977) and Perley & Butler (2013) for 3C286 is about 2.1 % at 1.47 GHz. The flux densities of sources 3C348 and 3C353 are taken from Baars et al. (1977) but these are known to less accuracy due to unknown contributions from temporal variation.

### 4.1 Boresight beam

A plot of the boresight  $\frac{T_{sys}}{\eta}$  vs frequency obtained from Virgo A, 3C286, 3C348 and 3C353 observations are shown in Fig. 7. The  $\frac{T_{sys}}{\eta}$  of ‘X’ and ‘Y’ polarizations range between 38 and 50 K at 1550 MHz with a median value of 45.5 K. The 1 sigma error on the estimated value range between 0.2 K, for the measurements toward Virgo A, and 1 K for the measurements toward 3C286. We formed beams using different 4.9 KHz wide spectral channel data and estimated error from the fluctuations

of  $\frac{T_{sys}}{\eta}$  over channels. Thus the quoted error does not include the uncertainty in the flux density of the source. When we used the injected tone to correct for any gain variation between on-source and off-source measurements, there was no appreciable change in the  $\frac{T_{sys}}{\eta}$ . Thus the origin of the variation of estimated  $\frac{T_{sys}}{\eta}$  using different celestial radio sources is not well understood and needs further investigation.

We estimated the receiver temperature ( $T_{rec}$ ) corresponding to the formed beam by applying the maximum SNR beamformer weights on the hot/cold load measurements made at the OTF. Since the measurement systems used for the two measurements are not identical, the receiver temperature for the formed beam will only be an approximate value. The estimated receiver temperature is shown in Fig. 8. The formed beam receiver temperature is about 25 K at 1.7 GHz.

## 4.2 Transferring beamformer weights from calibrator to target source

In a typical observation with PAF, it is required to estimate the beamformer weights on a strong calibrator source and then use these weights to form beams at the target source. We used the data set to investigate this ‘transfer’ of beamformer weights. Maximum SNR beamformer weights are obtained using Virgo A data set and applied on other observed calibrators to estimate  $\frac{T_{sys}}{\eta}$ . For comparison,  $\frac{T_{sys}}{\eta}$  is also obtained by solving for the weights using the calibrator data set, which could be done since these sources have flux density  $> 10$  Jy at 1.4 GHz. Fig. 9 shows the  $\frac{T_{sys}}{\eta}$  vs frequency obtained by transferring the weights from Virgo A data and those obtained by solving the weights using the data toward the target source. As seen in the figure the estimated values of  $\frac{T_{sys}}{\eta}$  using the two methods agree well within the estimation error. In Fig. 10, the maximum SNR beamformer weights obtained using data toward different sources are plotted. As seen from the figure, the beamformer weights do not sensitively depend on the position of the sources in the sky for January 25 data set. The elevation of the observed sources were between  $38^\circ$  and  $75^\circ$ . However, variation is seen between Virgo A data taken on January 25 and January 30. The January 30 data was taken after the cryostat was re-pumped and cooled. Note that we did not do a telescope positioning offset correction for January 30 observations, which can contribute to the change seen in the weights between the two days.

## 4.3 Off-boresight beams

Observations toward Virgo A were taken with  $\pm 4'.2$  position offset along elevation and cross elevation. This data set is used to form beams at these offset positions from boresight. Beams at these offset positions are also formed by maximizing SNR. A plot of  $\frac{T_{sys}}{\eta}$  vs frequency obtained for beams formed at different offsets from boresight are shown in Fig. 11. The difference in  $\frac{T_{sys}}{\eta}$  for the different offsets is about 4 K at 1550 MHz. Note that the FWHM beam width at 1550 MHz is  $7'.9$ .

## 5 $\frac{T_{sys}}{\eta}$ vs offset from boresight at 1700 MHz

The ‘grid observation’ toward Virgo A at 1.7 GHz were used to form beams at several different offsets from the boresight. The uppermost plot in Fig. 12 shows the grid positions along with sky positions (shown in red) where the maximum SNR beams were formed. The  $\frac{T_{sys}}{\eta}$  with radial offset from boresight is shown in the lowermost plot of Fig. 12. The half power beamwidth of the GBT at 1.7 GHz is  $7'.2$ . At this offset the  $\frac{T_{sys}}{\eta}$  is about 63 K for the ‘X’ polarization – i.e. it is about

13 K higher than the  $\frac{T_{sys}}{\eta}$  toward the boresight. The maximum SNR beamformer weights for 4 positions are shown in Fig. 13. As seen in Fig. 13, the weights have significant value for the 7 adjacent dipoles. At 6' offset from the boresight, the 7 elements that have the significant weight values are near the edge of the array. Thus we conclude that the ‘field of view’ of the PAF is being limited to about 6' due to the finite array size.

The receiver temperature estimated at different offset positions by applying beamformer weights at the corresponding position to the OTF measurements are shown in Fig. 8. The median value of the receiver temperature is about 25 K.

The shapes of the formed beams for three cross-elevation offsets (0.0', 3.0' and 6.0') are obtained from the ‘grid observation’. The maximum SNR beamformer weights obtained for each of these offsets are applied to grid data to get the beamshapes. The elevation and cross-elevation cuts of the beams are shown in Fig. 14.

## 6 Comparison of Survey speed of PAF with the GBT L-band system

The system temperature of the GBT L-band feed is 18.4 K at 1.7 GHz for typical galactic background and its aperture efficiency is 70 % (see GBT Proposer’s Guide 2015). Thus the  $\frac{T_{sys}}{\eta}$  of this feed is 26.3 K. This means that, for the PAF with 7 beams overlapping at the FWHM beamwidth of 7'.2 and taking  $\frac{T_{sys}}{\eta}$  of 63 K at 1.7 GHz at the FWHM beamwidth, the survey speed of the PAF exceeds the GBT L-band system by 20 %.

## 7 Comparison of measured $\frac{T_{sys}}{\eta}$ with PAF model

An electromagnetic and network model for the PAF was developed at the NRAO. Modeling starts with electromagnetic simulation of the array in the CST software package. This simulation provides the embedded beam patterns of the array elements and impedance matrix of the array. The rest of the modeling is done in Matlab. The receiver temperature is computed for a given set of weights using the impedance matrix and noise model of the amplifiers used in the array. The array is then placed at the prime focus of the GBT and the embedded patterns were used to compute the spillover and aperture efficiency matrices. For the same set of weights used for computing the receiver temperature, aperture and spillover efficiencies are obtained. The signal-to-noise ratio, defined as the ratio of the expected antenna temperature due to a source to the sum of the receiver, spillover temperature and sky temperature, is computed. The sky temperature is the sum of cosmic microwave background temperature (2.7 K) and galactic background radiation temperature. A solution for the weights that maximize the SNR is then obtained and these weights are used to get the best model  $\frac{T_{sys}}{\eta}$ . This computation is repeated for different frequencies. For the model results presented here, the mesh size used in CST is  $\frac{1}{10}$  of the wavelength and the embedded field patterns are sampled at 5°. Refined results for higher mesh resolution CST simulation and other modeling details will be presented in a future report.

We first compared the receiver temperature predicted by the model with the OTF measurements. The receiver temperature obtained from the model is about 6.4 K at 1.7 GHz due to the amplifier alone. Losses in the thermal transition are expected to add about 4 K, which gives a receiver temperature about 10.4 K at 1.7 GHz. We have replaced the transistors in the amplifier in 2013 and the noise model of these transistors are not available. The new transistors are expected to increase the noise temperature by about 5 K resulting in a receiver temperature of 15.4 K at 1.7

GHz. This receiver temperature is about 8 K lower than the measured value. The origin of this 8 K needs further investigation. Here we have parametrized the model results in terms of these 4 sets of receiver temperatures: LNA alone, LNA with thermal transition, LNA with thermal transition and added 5K transistor noise, and all of the above with an additional 8K.

### 7.1 Comparison of boresight beam $\frac{T_{sys}}{\eta}$ with PAF model

Fig. 15 shows the  $\frac{T_{sys}}{\eta}$  vs frequency for the 4 sets of receiver temperatures mentioned above. A galactic background temperature of 0.7 K at 1.42 GHz is obtained from the off-source position (see Table 3) near Virgo A (Reich & Reich 1986). This background temperature is scaled with a spectral index  $-2.7$  to get the model sky temperature at different frequencies. As seen in Fig. 15, the model values for  $\frac{T_{sys}}{\eta}$  are close to the measured value if the formed beam receiver temperature is about 24 K at 1.7 GHz. This receiver temperature is comparable with the value shown in Fig. 7 at 1.7 GHz. The model frequency response show similarity with the measured response, however, it does not reproduce the measured frequency response to a great accuracy.

The aperture efficiency predicted by the model is about 70 % at 1.7 GHz for receiver temperature 24 K. The spillover efficiency obtained from the model is shown in Fig. 15. For receiver temperatures close to 24 K, the spillover efficiency is about 98%. The array simulation in CST does not take into account electromagnetic scattering from structures of the GBT. Further investigation is needed to check whether higher spillover efficiencies, as indicated by the lower receiver temperature models, can be achieved in practice.

The beamformer weights at 1.7 GHz obtained from the PAF model along with those obtained from measurements are shown in Fig. 16. The model weights have significant value for the center element and the 7 neighboring elements. The weights estimated from measurements show similar behavior, but these values are affected by relative sensitivity of different signal paths in PAF. Further, any telescope pointing offset will contribute to the difference between the two set of weights.

### 7.2 Comparison of Off-boresight beam $\frac{T_{sys}}{\eta}$ with PAF model

The PAF model was used to estimate the  $\frac{T_{sys}}{\eta}$  for different offsets from boresight. Fig. 17 shows the model  $\frac{T_{sys}}{\eta}$  at 1.7 GHz vs offset angle. The model values are shown for different receiver temperatures, marked on the figure, at 1.7 GHz. For comparison, the measurements at the same frequency are shown in the figure. The model with receiver temperature about 24 K at 1.7 GHz agrees well with the model.

The model receiver temperature at 1.7 GHz vs offset angle is shown in Fig. 17. As seen in the figure the receiver temperature is independent of offset angle. Approximate receiver temperature for offset angle from OTF measurements were obtained using the beamformer weights estimated from Virgo A observations. These values are shown in Fig. 8 as a function of offset angle. The receiver temperature obtained from OTF measurements is also independent of offset angle, although there is a large scatter in values (about 15 K peak to peak).

## 8 Conclusion and Future direction

The report gives a brief description of the PAF test setup, the OTF measurements, observations made on the GBT, and results. The beams are formed by maximizing SNR. Our main conclusions are:

- The measured  $\frac{T_{sys}}{\eta}$  of the boresight beam of PAF on the GBT range from 38 K to 50 K at 1550 MHz with a median value of 45.5 K.
- The measured receiver temperature of each dipole in PAF is about 25 K at 1700 MHz. The median formed beam receiver temperature is also about 25 K at 1700 MHz.
- We demonstrate that the beamformer weights, obtained from observations toward a strong calibrator, can be used for target source observations without loss of any performance.
- The derived beamformer weights are stable and repeatable over a large range of elevation and azimuth of the telescope.
- The  $\frac{T_{sys}}{\eta}$  increase for off-axis beams spaced at 1 full-width half-maximum (FWHM) spacing was 13K, increasing from 50K to 63K at 1 FWHM beamwidth (7'.2) offset from boresight at 1700 MHz.
- The modeled results predict well the measured  $\frac{T_{sys}}{\eta}$  vs offset from boresight direction but needs an increase in receiver temperature of about 8K to match the measured results. Additionally, there is an increase of about 5K in receiver temperature that came from the use of replacement transistors in the low-noise amplifiers. The model also predicts the measured  $\frac{T_{sys}}{\eta}$  vs frequency with the additional increase in receiver temperature mentioned above.

A summary of issues that need further investigation are listed below.

- The discrepancy between the modeled and measured receiver temperature will be investigated by test and analysis.
- Further investigation is needed to understand the spread in  $\frac{T_{sys}}{\eta}$  when measured using different sources.
- Upgrades to the instrumentation are underway including improved low-noise amplifiers, digital fiber link, and higher bandwidth real-time digital backend.

## Acknowledgment

We acknowledge very useful discussions and suggestions from Matt Morgan, Robert Dickman and S. K. Pan during the course of this work. We thank Morgan McLeod for giving comments on the manuscript and J. D. Nelson for providing help with the installation of PAF system.

## Reference

- Baars, J. W. M., et al. , 1977, A&A, 61, 99  
 Warnick, K. F., et al. , 2011, IEEE Trans. Antennas Propag., 59, 1876  
 Perley, R. A., Butler, B. J., 2013, ApJS, 204, 19  
 Reich, P., Reich, W., 1986, A&AS, 63, 205



Figure 1: Image of “Kite” dipole is shown on the left and the 19 element dual-polarization “Kite” array on the right.

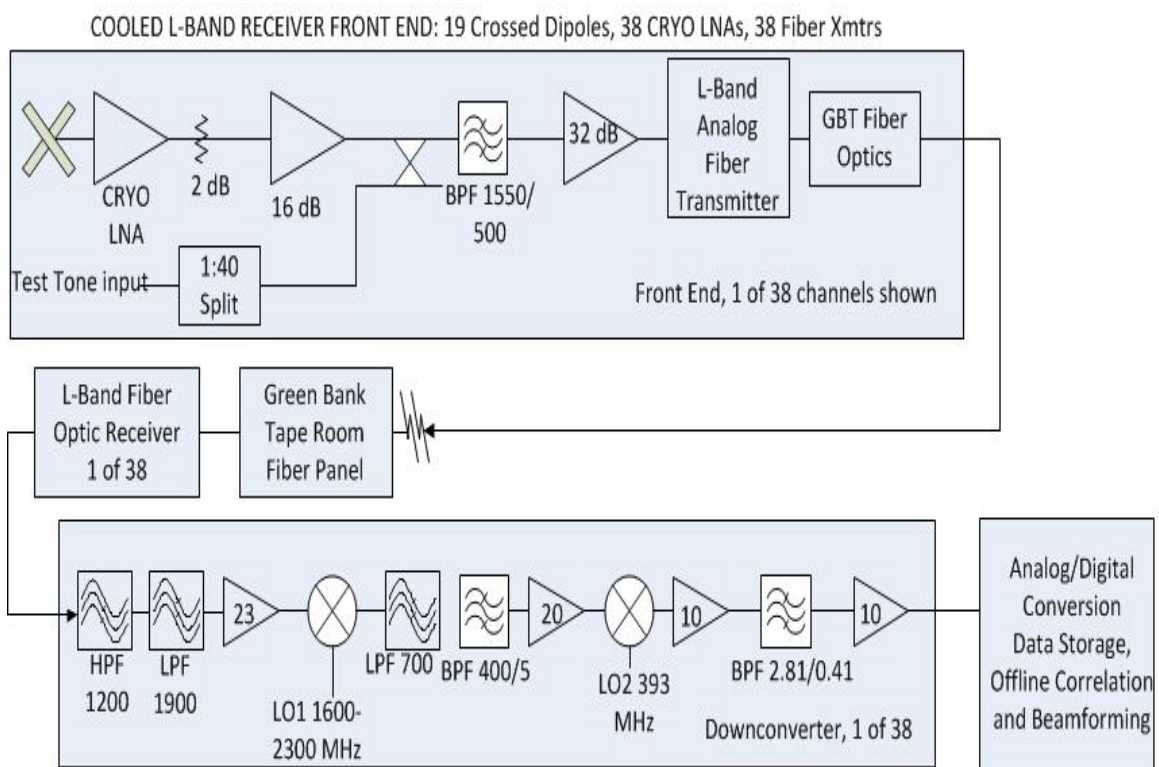


Figure 2: Simplified block diagram of the PAF receiver system and backend used for January 2015 observations.

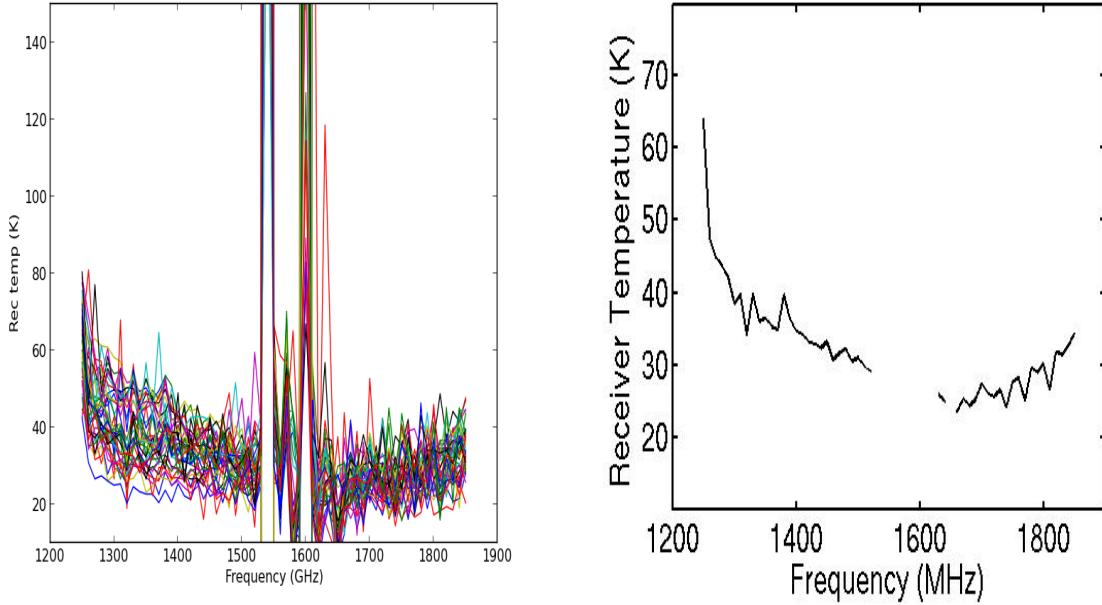


Figure 3: PAF receiver temperature vs frequency as measured in the OTF. Measured receiver temperatures at each frequency of all the 38 dipoles in the array are shown on the left and the median receiver temperature of 38 dipoles at each frequency is shown on the right. At frequencies near 1600 MHz, the measurements were affected by radio frequency interference.

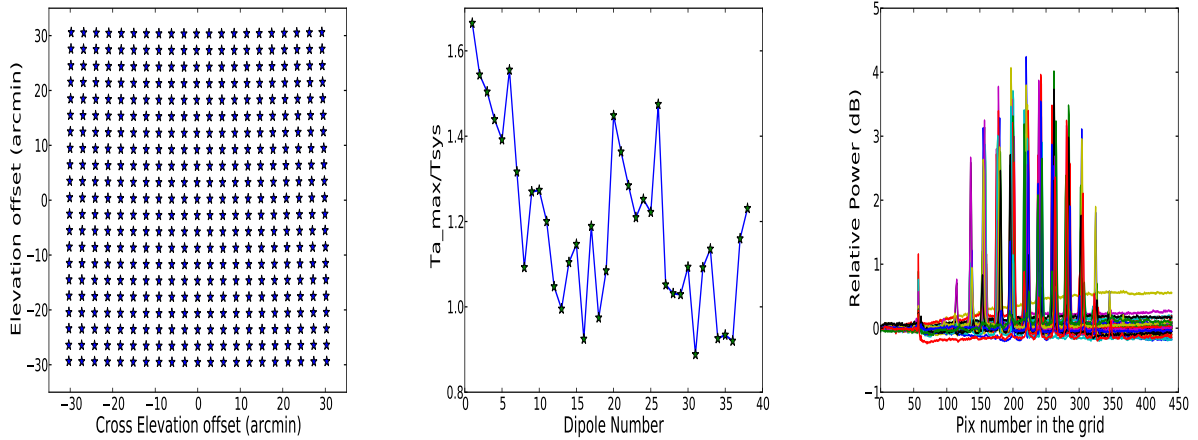


Figure 4: **Left:** The observed grid positions are shown in the figure. The grid position (0,0) corresponds to the source position Virgo A. **Middle:** The peak ratio of antenna temperature due to the 19x2 dipoles to system temperature in the grid observations. All the dipoles show deflection on Virgo A. A major contribution to the variation of  $T_{a,max}/T_{sys}$  across dipoles is because the peak of each dipole beam is not sampled in the grid observations. **Right:** Output power relative to an off-source grid position for each dipole vs position on the grid. This plot shows that the gain variation is less than 0.5 dB over 2.5 hrs or so.

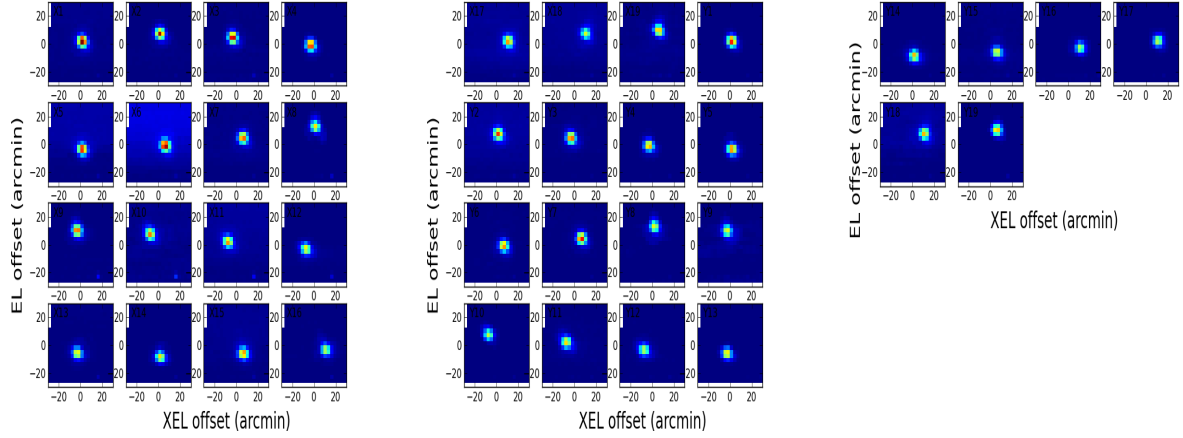


Figure 5: Beam patterns obtained from the 19x2 dipole outputs. The ‘grid observation’ toward Virgo A was used to obtain the beam patterns. The color scale represent  $T_a/T_{sys}$  and is set to 0 to 1.5 for all the plots.

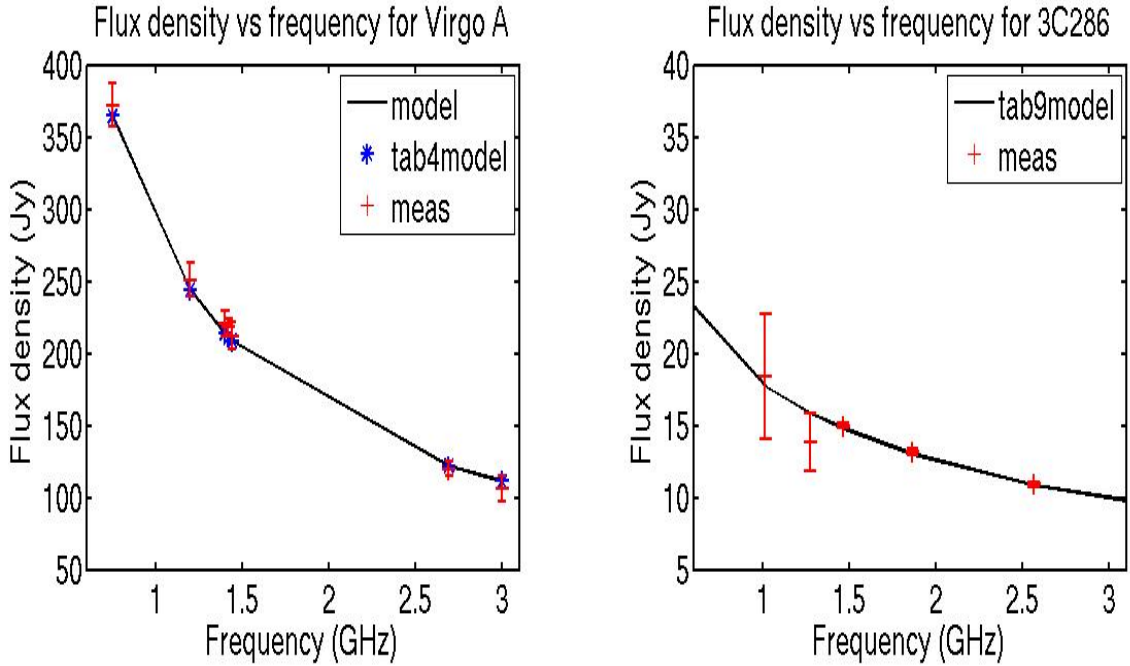


Figure 6: Models for the flux density vs frequency for Virgo A (left) and 3C286 (right). The flux density model for Virgo A is from Baars et al. (1977) and for 3C286 is from Perley & Bulter (2013). The measured values given in the two references with 1 sigma error bars are also shown.

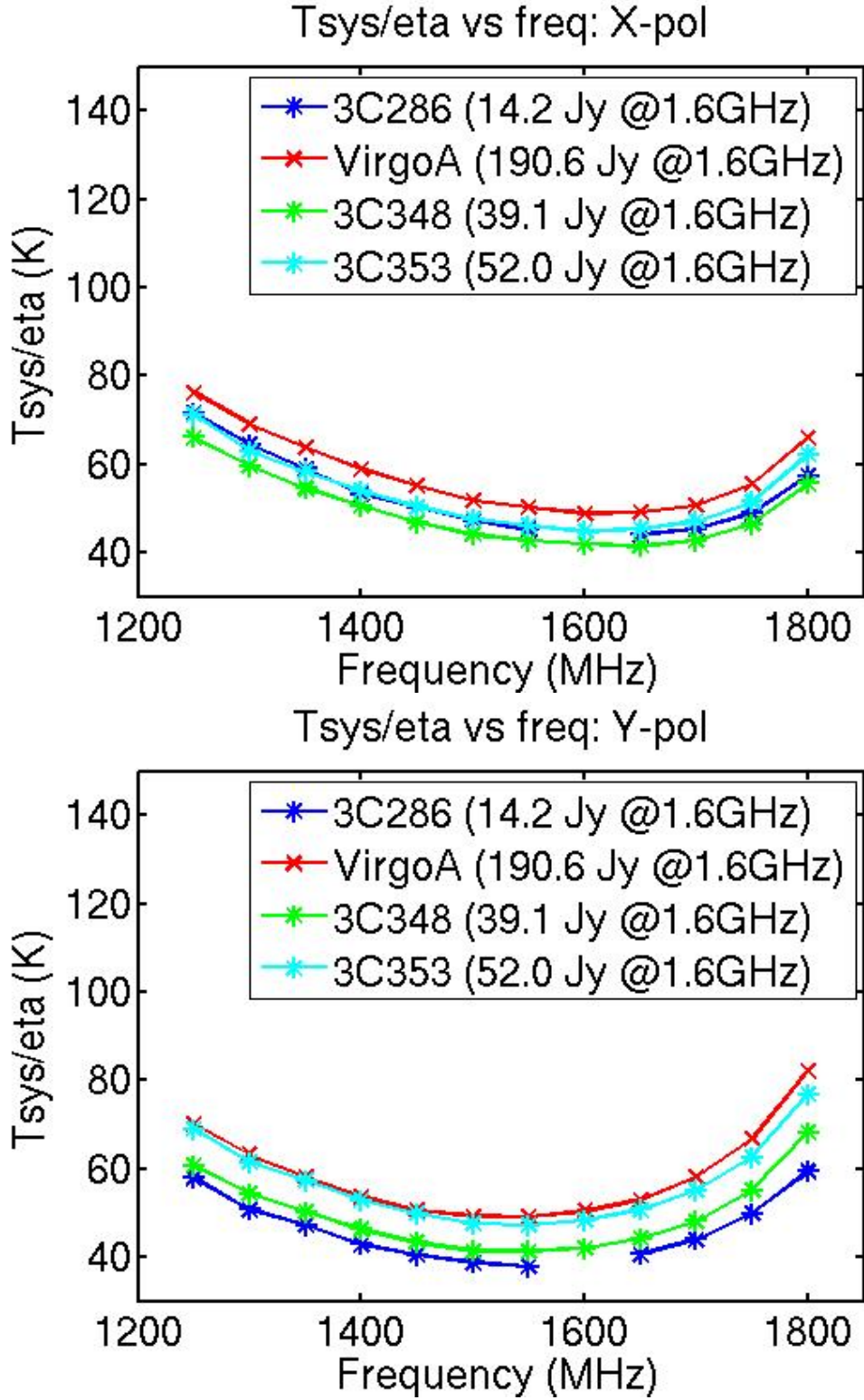
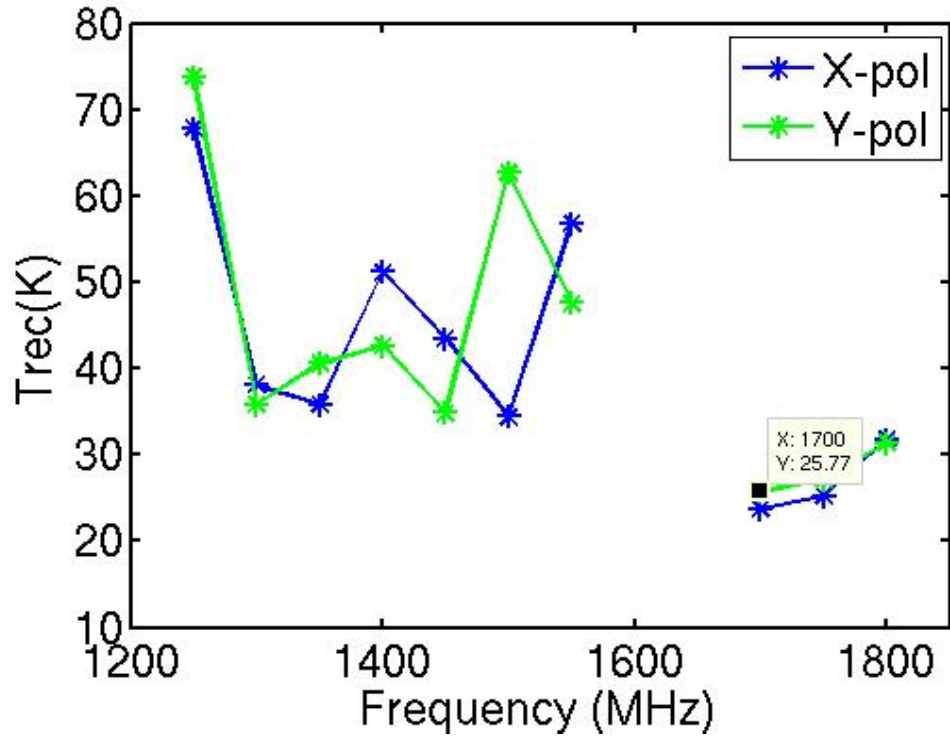


Figure 7: Measured  $\frac{T_{sys}}{\eta}$  vs frequency for maximum signal-to-noise ratio boresight beam. Results from “X” and “Y” polarization data are shown on the top and bottom respectively. Estimated 1 sigma error for these measurements range from 0.2 K (for Virgo A) to 1 K (for 3C286). The azimuth and elevation of the sources during observations were : Virgo A (229°, 56°), 3C286 (242°, 75°), 3C348 (130°, 45°) and 3C353 (130°, 38°).



Trec vs beam offset (1.7 GHz)

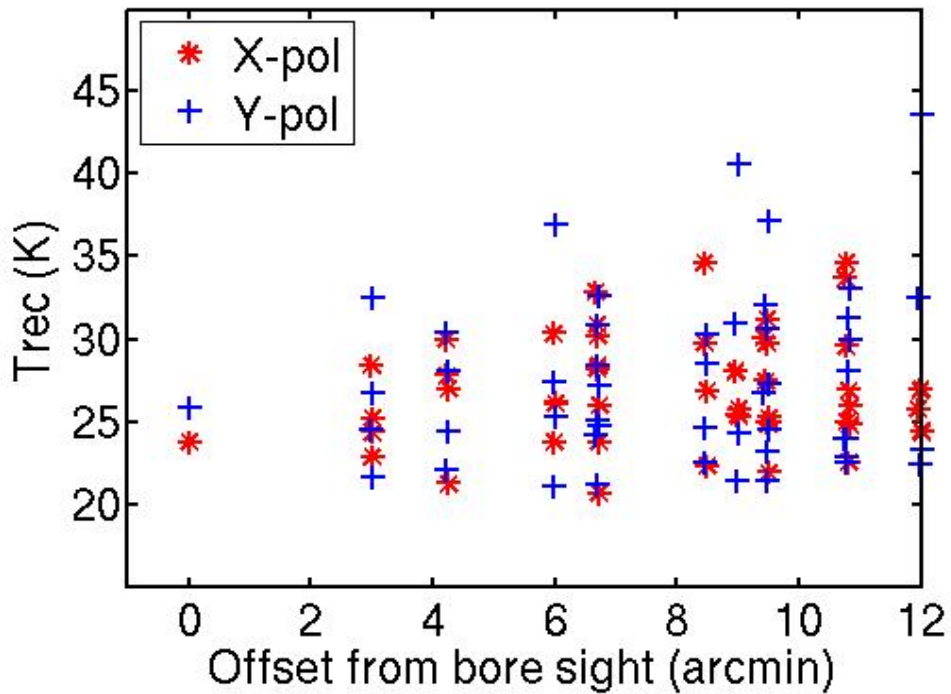


Figure 8: **Top:** Receiver temperature vs frequency. The receiver temperature is approximately obtained by applying the maximum SNR beamformer weights to the OTF measurements (see text). **Bottom :** Receiver temperature vs offset from boresight. The maximum SNR beamformer weights obtained at each offset position is applied to the OTF measurements to get an approximate receiver temperature (see Section 5).

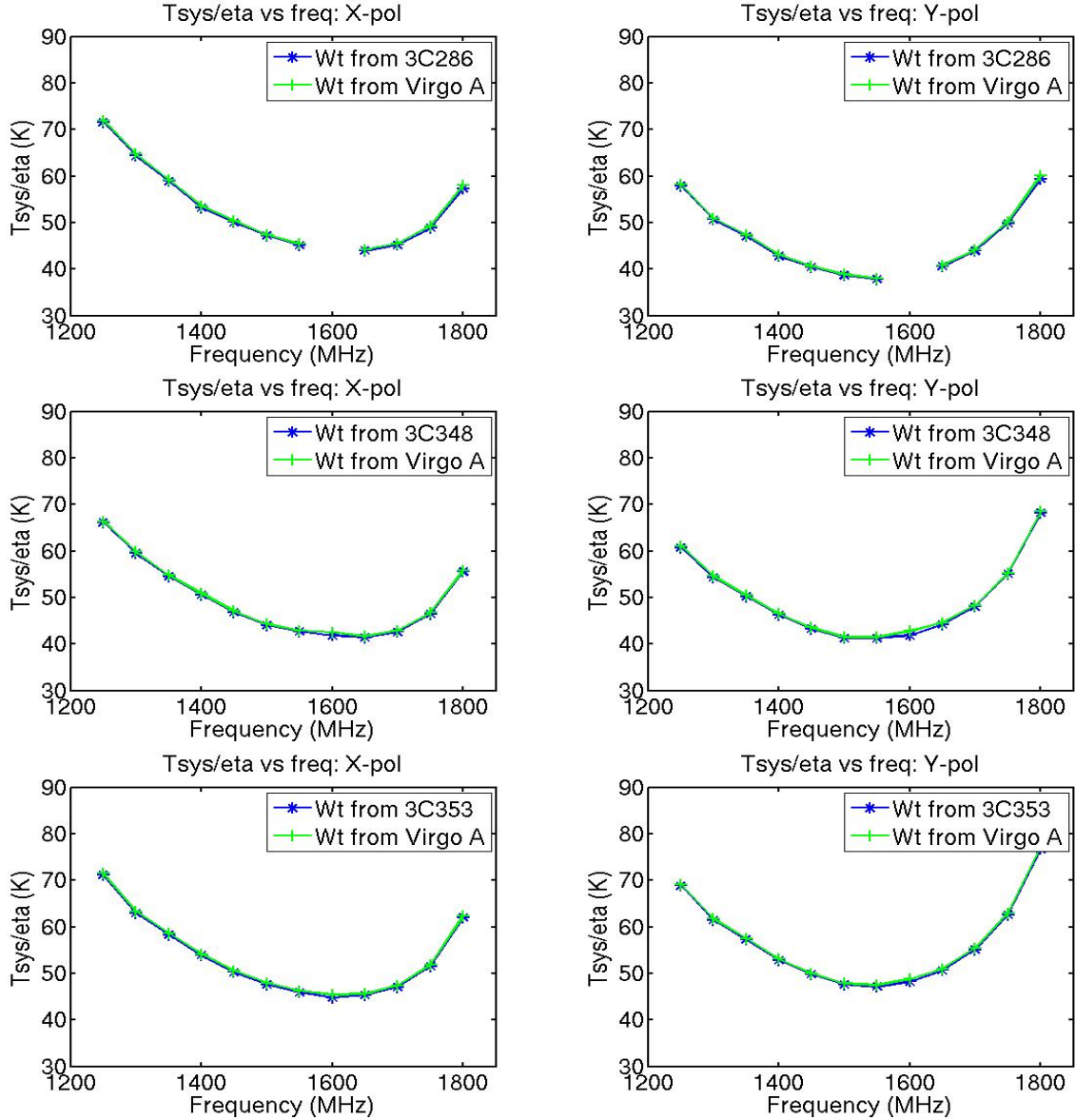


Figure 9: Measured  $\frac{T_{sys}}{\eta}$  vs frequency for maximum SNR beamformer. Results for “X” polarization are shown on the left and those for the “Y” polarization are shown on the right. The blue curve shows the  $\frac{T_{sys}}{\eta}$  obtained by solving maximum SNR beamformer weights on the sources shown in the legend. The green curve shows the  $\frac{T_{sys}}{\eta}$  obtained by applying the weights obtained from Virgo A data. The azimuth and elevation of the sources were : Virgo A (229°, 56°), 3C286 (242°, 75°), 3C348 (130°, 45°) and 3C353 (130°, 38°)

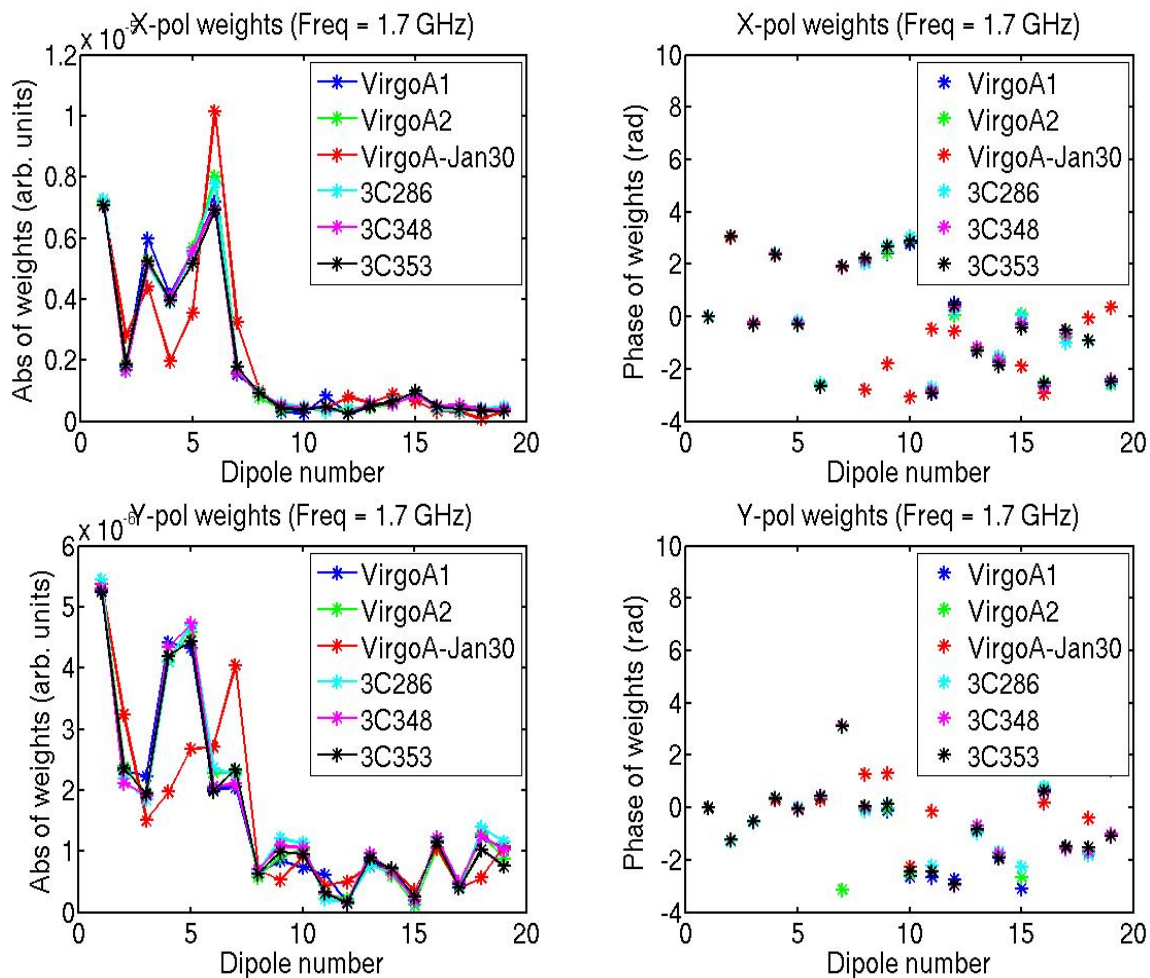
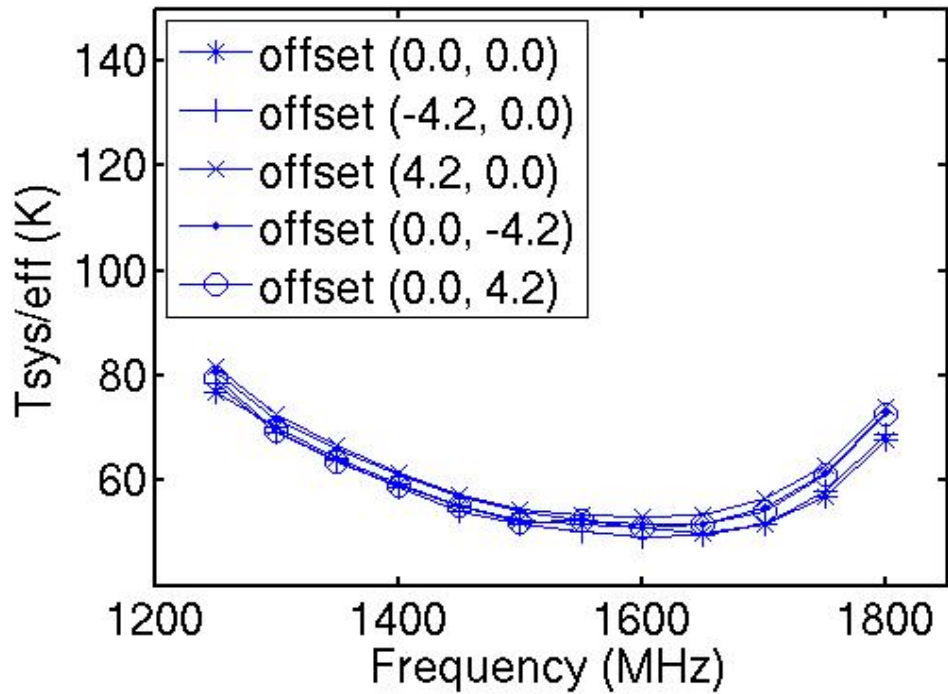


Figure 10: Estimated maximum SNR weights for different sources. The absolute value of the weights obtained from “X” and “Y” polarization data set are shown on the top-left and bottom-left plots respectively. The phase of the weights for these polarizations are shown on the top-right and bottom-right respectively. The weights labeled as ‘VirgoA1’, ‘VirgoA2’, ‘3C286’, ‘3C348’ and ‘3C353’ correspond to data taken on January 25. The source elevations during the observations range between  $38^\circ$  and  $75^\circ$ . The weights labeled as ‘VirgoA-Jan30’ correspond to data taken on January 30, 2015 after the cryostat were re-pumped and cooled.

### Performance of off-bore sight beams (X-pol)



### Performance of off-bore sight beams (Y-pol)

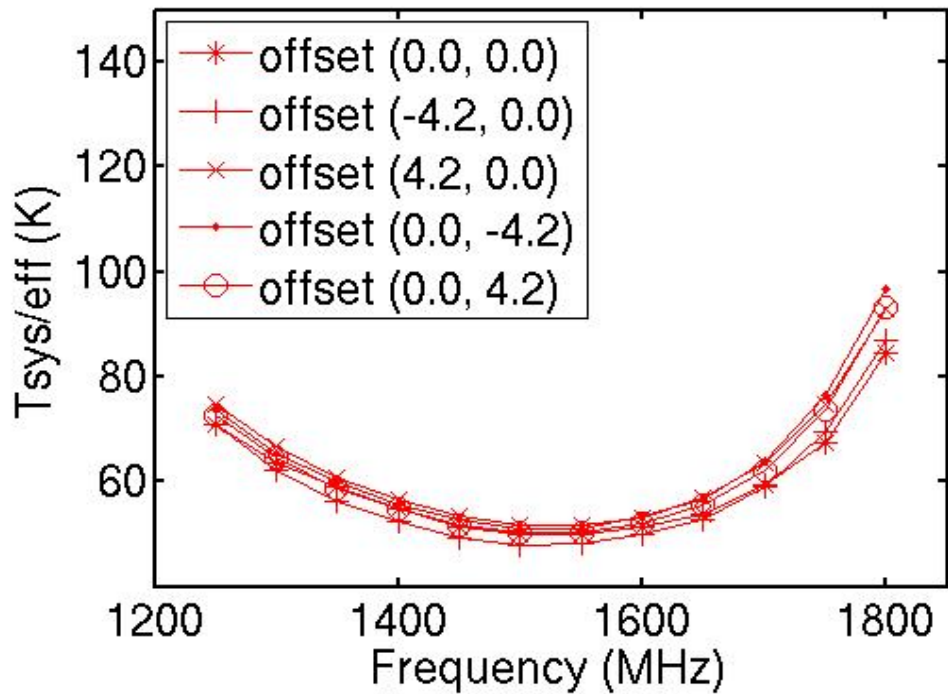
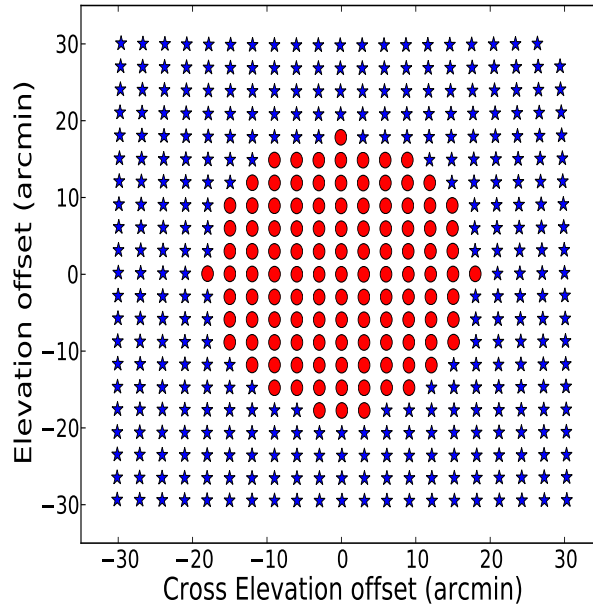


Figure 11: Measured  $\frac{T_{sys}}{\eta}$  vs frequency for maximum SNR beams formed at the offset positions indicated on the figure. Results for “X” polarization are shown on the top and those for the “Y” polarization are shown on the bottom. Estimated 1 sigma error for these measurements is about 0.2 K.



Tsys/eff vs beam offset (1.7 GHz)

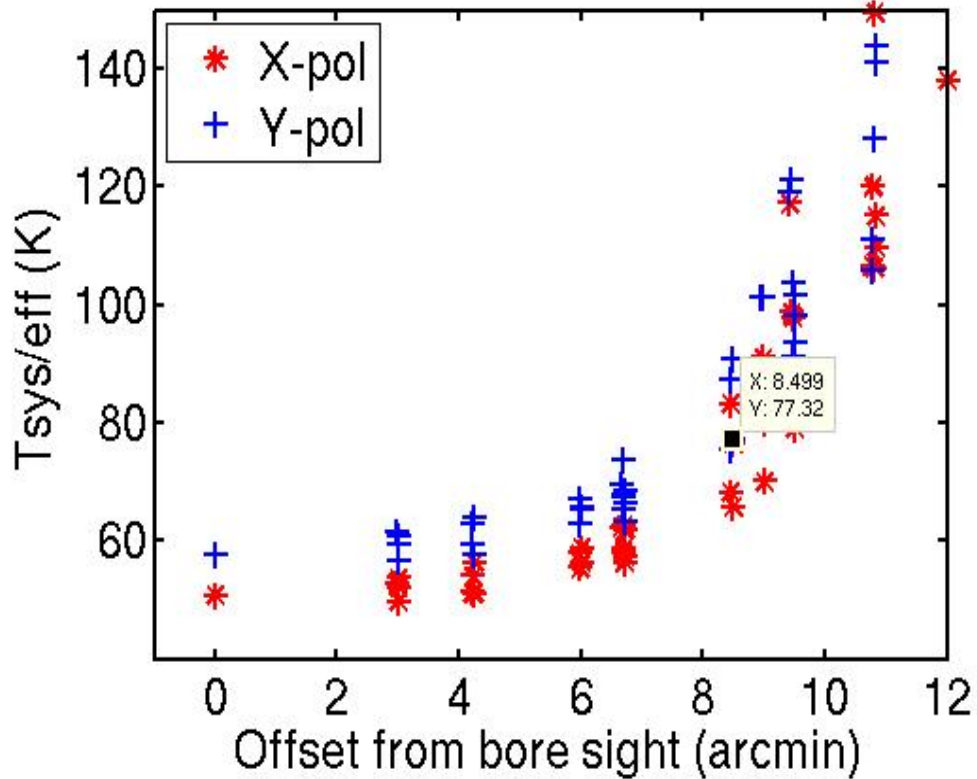


Figure 12: **Top:** Positions (after removing the offset at Virgo A position) observed during the ‘grid observation’ at 1.7 GHz.  $\frac{T_{sys}}{\eta}$  is estimated by maximizing the SNR at the positions marked in red. **Bottom:**  $\frac{T_{sys}}{\eta}$  vs radial offset from the center of the grid. The estimated value for  $\frac{T_{sys}}{\eta}$  at 7.2 (FWHM beam width at 1.7 GHz) is about 63 K. The 1 sigma error on the estimated  $\frac{T_{sys}}{\eta}$  at positions < 8’ is on the average about 0.4 K.

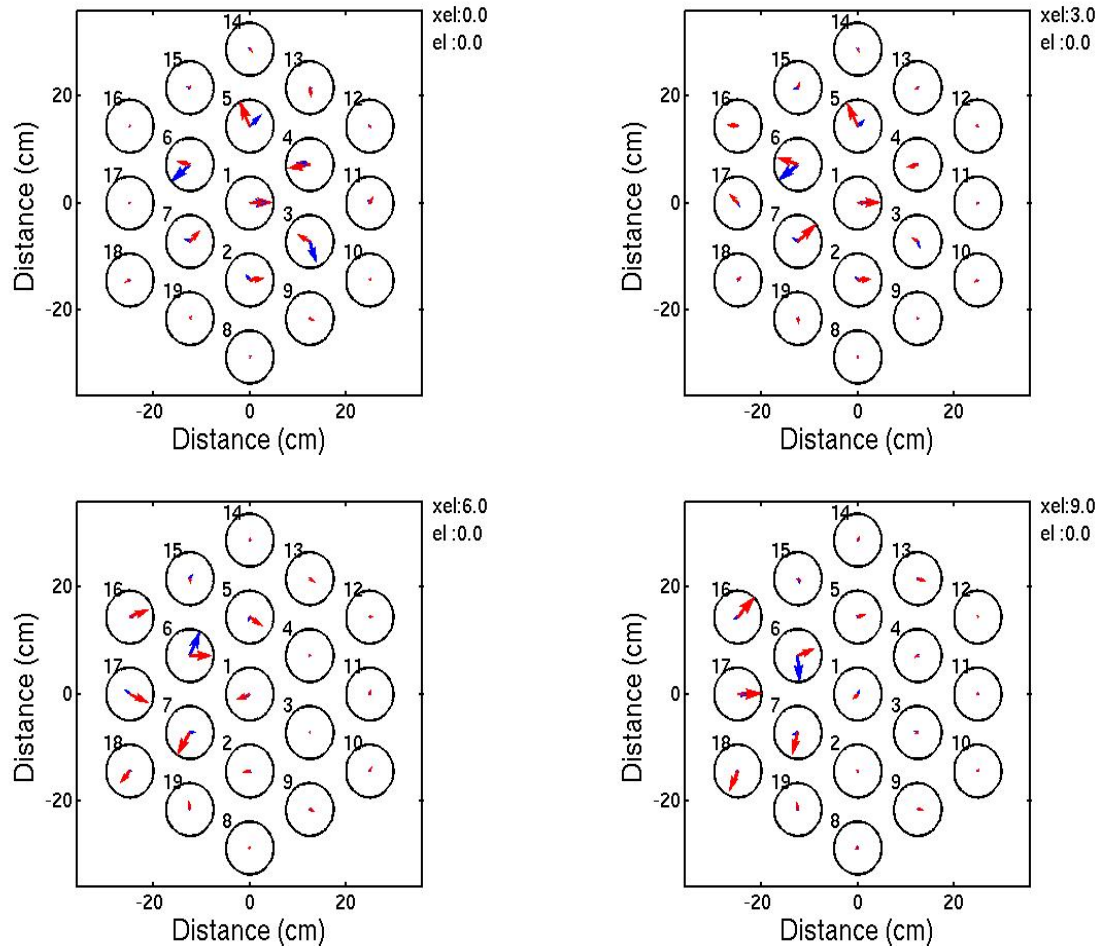


Figure 13: Beamformer weights for different offsets from boresight. The cross elevation (xel) and elevation (el) offsets are marked on the top right corner. The length of the arrow is the normalized magnitude of the weight and the phase of the complex number is represented by the angle northward from east direction. The normalization of weight is with respect to the maximum absolute value of the 19 weights. Weights for 'X' polarization is shown in blue and those for 'Y' polarization is shown in red. The radius of the circle represents unit weight and the center of the circles corresponds to the physical location of the dipole elements in PAF.

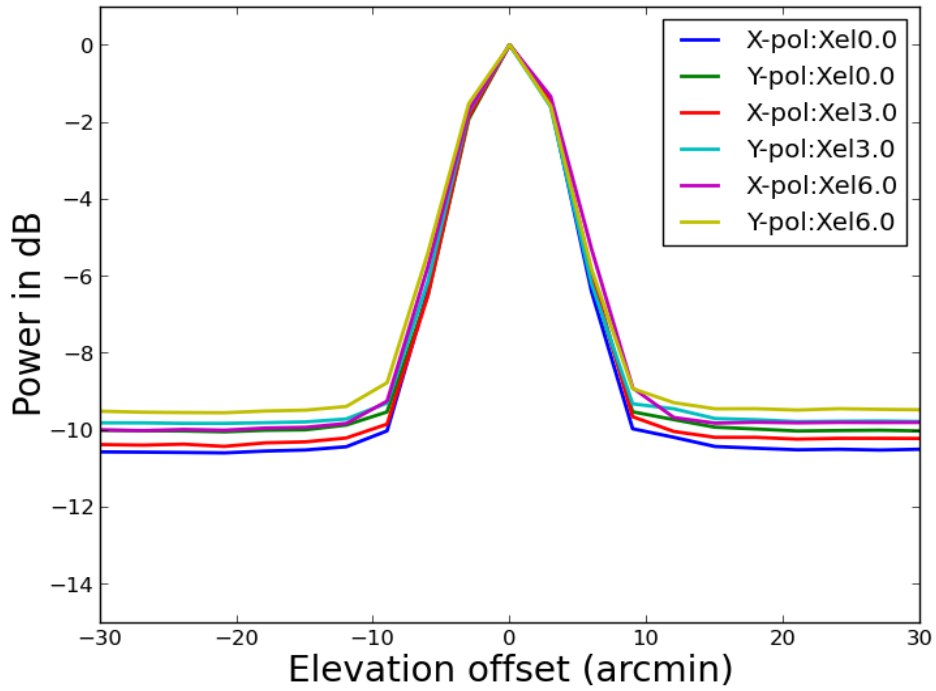
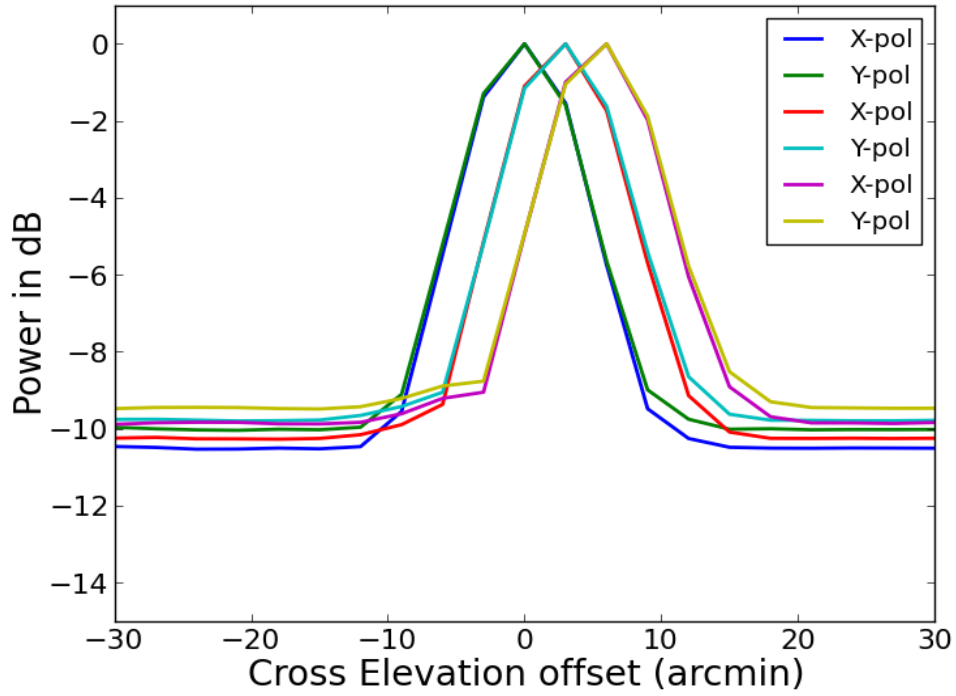


Figure 14: Shapes of the formed beams at cross-elevation offsets  $0.0'$ ,  $3.0'$  and  $6.0'$ . The beamshapes are obtained using the 'grid observation' toward Virgo A at 1.7 GHz. The cross-elevation and elevation cuts of the beams are shown in the top and bottom figures respectively.

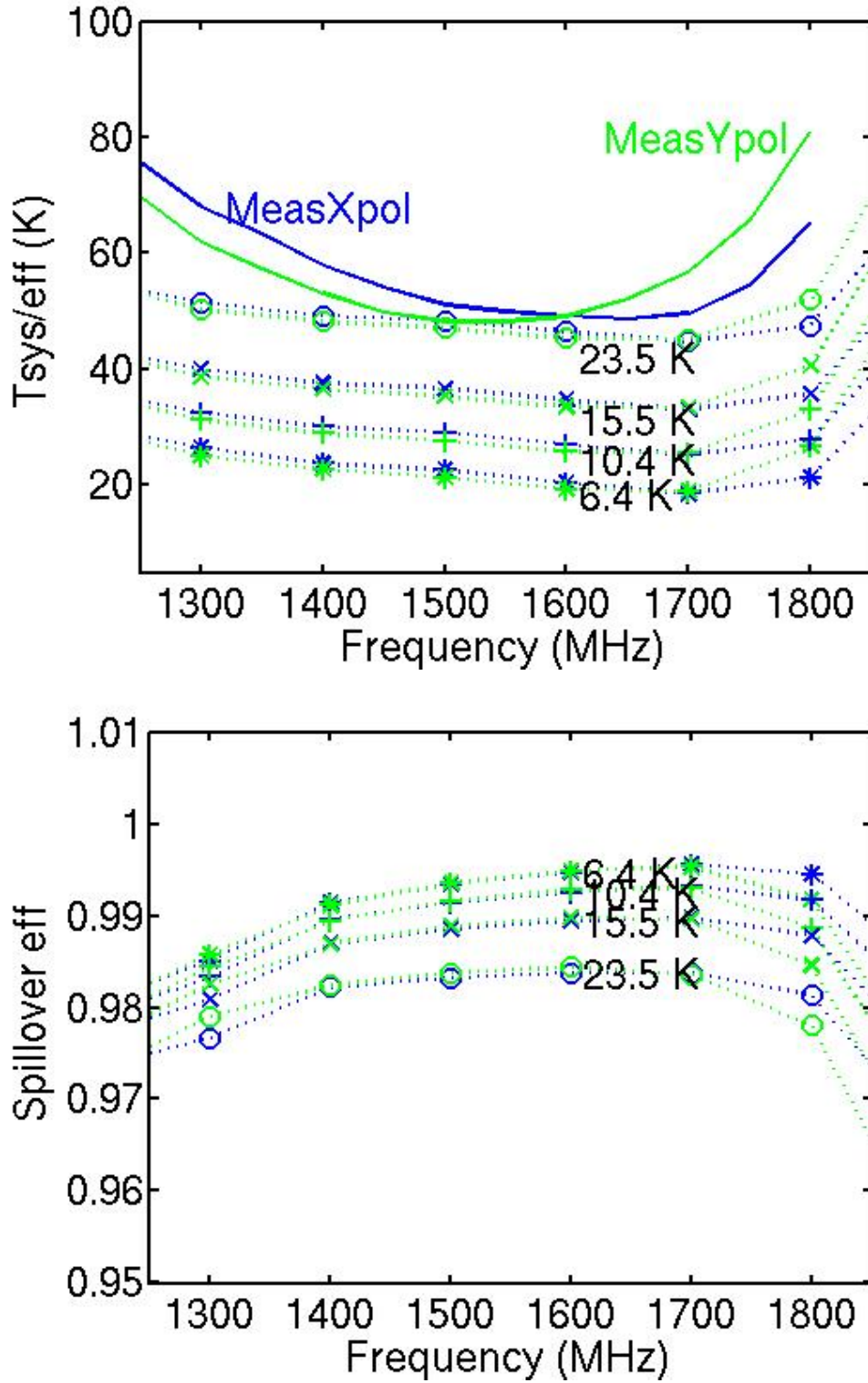


Figure 15: **Top:**  $\frac{T_{sys}}{\eta}$  vs frequency from PAF model (dotted line) and measurement (solid line). The model  $\frac{T_{sys}}{\eta}$  is calculated for different receiver temperature (see text for details). The receiver temperature of each set of models at 1.7 GHz is marked on the plot. **Bottom:** Estimated spillover efficiency from the same set of models.

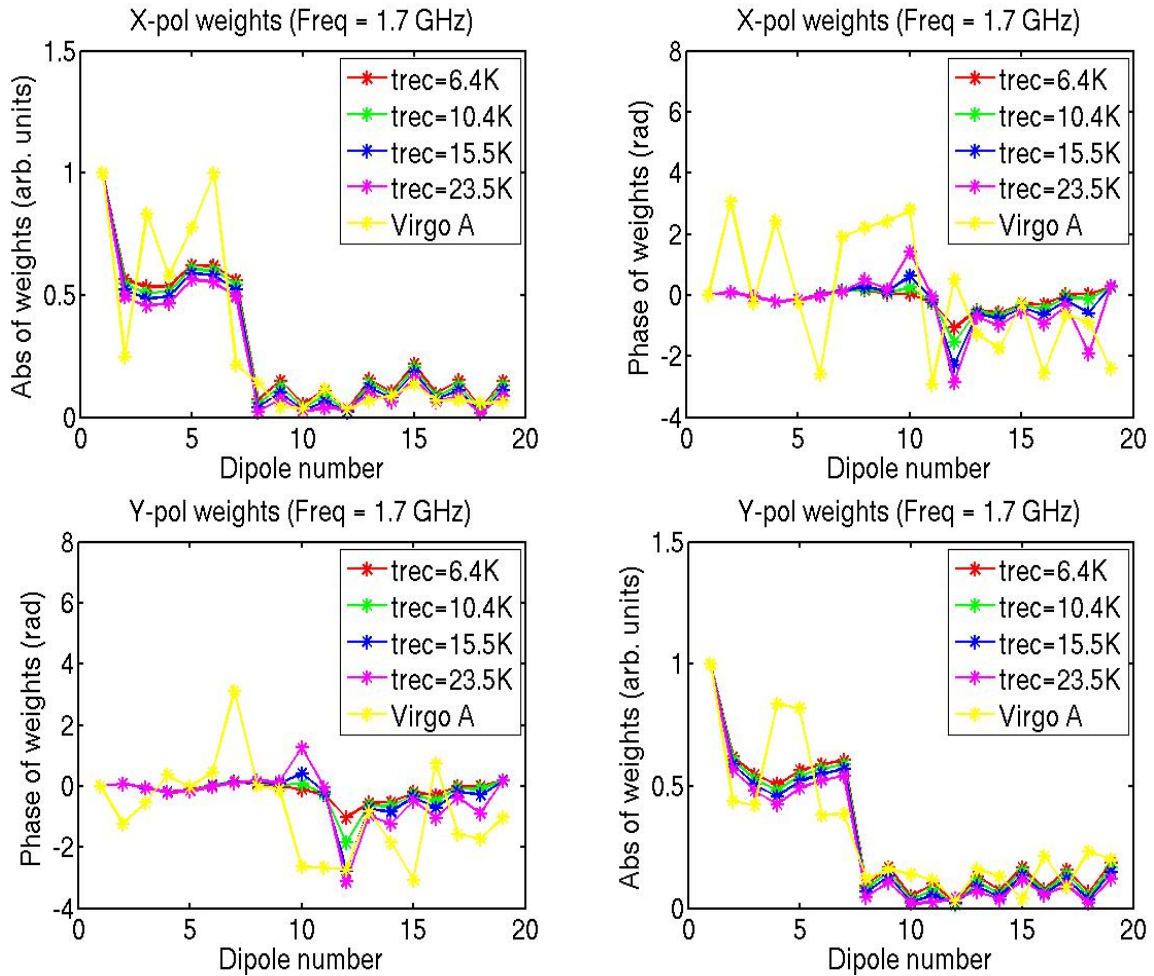


Figure 16: Comparing beamformer weights at 1.7 GHz from PAF model and those obtained from observations. The absolute value of the weights for “X” and “Y” polarizations are shown on top-left and bottom-left respectively. The phase of the weights for these polarizations are shown on top-right and bottom-right respectively. The weights are normalized with the value for dipole 1 for comparison with model weights. The model beamformer weights are plotted for the different receiver temperature at 1.7 GHz marked on the plot. The estimated weights are from Virgo A data set.

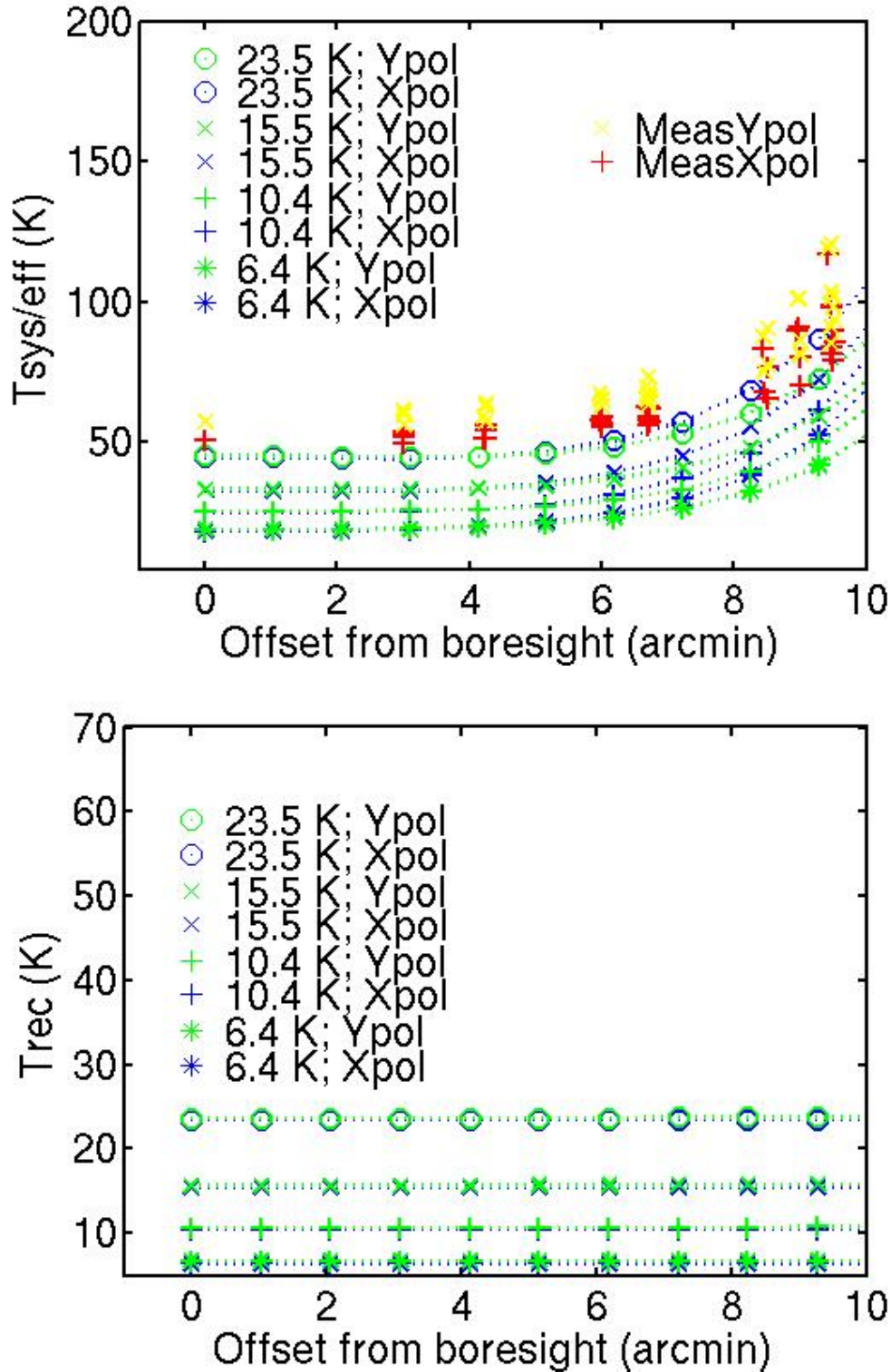


Figure 17: **Top:**  $\frac{T_{sys}}{\eta}$  vs frequency from PAF model (dotted line) and measurement (solid line). The model  $\frac{T_{sys}}{\eta}$  is calculated for different receiver temperature (see text for details). The receiver temperature of each set of model at 1.7 GHz is marked on the plot. **Bottom:** Estimated receiver temperature from the same set of models.